University of South Carolina
Scholar Commons

Faculty Publications | Mechanical Engineering, Department of

1-31-2019

High-Throughput 3D Reconstruction of Stochastic Heterogeneous Microstructures in Energy Storage Materials

Yanxiang Zhang

Mufu Yan

Yanhong Wan

Zhenjun Jiao

Yu Chen

See next page for additional authors

Follow this and additional works at: https://scholarcommons.sc.edu/emec_facpub

 Part of the Mechanical Engineering Commons

Publication Info

Published in *npj Computational Materials*, Volume 5, 2019.

This Article is brought to you by the Mechanical Engineering, Department of at Scholar Commons. It has been accepted for inclusion in Faculty Publications by an authorized administrator of Scholar Commons. For more information, please contact digres@mailbox.sc.edu.

Author(s)

Yanxiang Zhang, Mufu Yan, Yanhong Wan, Zhenjun Jiao, Yu Chen, Fanglin Chen, Changrong Xia, and Meng Ni

This article is available at Scholar Commons: https://scholarcommons.sc.edu/emec_facpub/834

npj | Computational Materials

www.nature.com/npjcompumats

ARTICLE OPEN

High-throughput 3D reconstruction of stochastic heterogeneous microstructures in energy storage materials

Yanxiang Zhang[1], Mufu Yan[1], Yanhong Wan[2], Zhenjun Jiao[3], Yu Chen[4], Fanglin Chen[5], Changrong Xia[2] and Meng Ni[6]

Stochastic heterogeneous microstructures are widely applied in structural and functional materials, playing a crucial role in determining their performance. X-ray tomography and focused ion beam serial sectioning are frequently used methods to reconstruct three-dimensional (3D) microstructures, yet are demanding techniques and are resolution-limited. Here, a high-throughput multi-stage 3D reconstruction method via distance correlation functions is developed using a single representatively large-sized 2D micrograph for stochastic microstructures, and verified by X-ray micro-tomography datasets of isotropic and anisotropic solid oxide fuel cell electrodes. This method provides an economic, easy-to-use and high-throughput approach for reconstructing stochastic heterogeneous microstructures for energy conversion and storage devices, and can readily be extended to other materials.

npj Computational Materials (2019)5:11 ; https://doi.org/10.1038/s41524-019-0149-4

INTRODUCTION

Solid oxide fuel cells (SOFCs) are developed world wide for clean and efficient electricity generation from fuels such as hydrogen, natural gas, gasoline, coal, and even biomass. In the past several decades, significant efforts have been made to the development of advanced electrode materials for durable, fuel flexible, and efficient operation of SOFC at reduced temperatures.[1] In addition, development of advanced electrode microstructures, with abundant electrochemically active sites, high catalytic activity, and stability, has been another major direction of research; however, a long-standing challenge.[2–5] There are difficulties in probing and controlling the complex microstructures. Morphologies and distributions of the heterogeneously interpenetrating percolating networks of materials, nanoscale internal surfaces and interfaces, and three-phase boundaries (TPBs) are very sensitive to the processing histories[6–9] and working conditions,[10–12] while playing crucial roles in determining electrode performance.[13,14] Therefore, quantification of electrode microstructures is critical for understanding the processing–microstructure–performance relationship and designing high-performance SOFCs. To this point, two-dimensional (2D) stereological methods have been employed to quantify electrode geometric characteristics.[15,16] However, this method is limited to the isotropic microstructures, and incapable of determining tortuosity factors and the percolated portions of the phase networks, surfaces, interfaces, and TPBs. Over the past decade, X-ray nanotomography (XNT) and focused ion-beam serial sectioning-scanning electron microscopy (FIB-SEM) have been employed to image the three-dimensional (3D) microstructures of SOFC electrodes.[15,17–22] However, both XNT and FIB-SEM show limited spatial resolution (typical 10–50 nm), which is insufficient to image the nanofeatures (<50 nm) of SOFC electrodes; for instance, the infiltrated/precipitated or in situ exsoluted nanoparticles and boundaries between phases of different functionalities.

Therefore, developing economic, easy-to-use, and super-resolution technologies for the 3D reconstruction is far from trivial. A potentially alternative technology is the stochastic reconstruction based on distance correlation functions (DCFs). Theoretically, this principle is capable of reconstructing stochastic 3D microstructures using a single 2D micrograph, which is easy to reach super-resolutions using 2D imaging technologies, such as scanning electron micrographs. The proof of concept, algorithm, and applications to reconstruction of porous media have been developed by Quiblier,[23] Torquato and co-workers,[24–29] and is first introduced to reconstruct a porous Ni-YSZ anode by Suzue et al. in 2008;[30] however, it has been rarely applied to SOFCs, and other energy devices where the stochastic microstructures are being extensively used. There are several challenging issues regarding the algorithm. The first issue concerns the computational efficiency. The basic idea of the algorithm is to exchange two voxels of different phases in a randomly generated voxel matrix so that its DCFs converge to the objective DCFs of the 2D micrograph. The two-point exchanging procedure is extremely inefficient for big volumes. For a typical volume dimension obtained by XNT and FIB-SEM, say $400 \times 400 \times 400$ voxels, the convergence will be computationally intractable. At present, the feasible size of volume is around $150 \times 150 \times 150$ voxels,[24–30] which is insufficient to represent statistically big volumes with 10 nm and higher resolutions. The second issue concerns the robustness. It is not verified that if the reconstructed volume has

[1]National Key Laboratory for Precision Hot Processing of Metals, MIIT Key Laboratory of Advanced Structure-Function Integrated Materials and Green Manufacturing Technology, School of Materials Science and Engineering, Harbin Institute of Technology, 150001 Harbin, China; [2]CAS Key Laboratory of Materials for Energy Conversion, Department of Materials Science and Engineering, University of Science and Technology of China, 230026 Hefei, China; [3]College of Science, Harbin Institute of Technology, 518055 Shenzhen, China; [4]Center for Innovative Fuel Cell and Battery Technologies, School of Materials Science and Engineering, Georgia Institute of Technology, Georgia, GA 30332-0245, USA; [5]Department of Mechanical Engineering, University of South Carolina, Carolina, SC 29205, USA and [6]Building Energy Research Group, Department of Building and Real Estate, The Hong Kong Polytechnic University, Hung Hom, Kowloon, Hong Kong
Correspondence: Yanxiang Zhang (hitzhang@hit.edu.cn) or Mufu Yan (yanmufu@hit.edu.cn)

Received: 30 August 2018 Accepted: 8 January 2019
Published online: 31 January 2019

the same statistical information with the real microstructure. If yes, it is not clear what degree the tolerance of DCFs should be converged to so that the geometric properties of the reconstructed volume can represent their realistic values. The third issue concerns the applicability. Similar to the difficulty encountered when using stereological method, the algorithm is currently limited to reconstructing isotropic structures. Although most of SOFC electrodes are isotropic produced by mixing-sintering of powders and infiltration of solution, some innovative anisotropic microstructures produced by, for example, freeze-drying and phase inversion have demonstrated promising performance. Thus, there is a need to generalize the algorithm.

Recently, several promising algorithms, such as cellular automata,[31] Markov random fields,[32] and truncated plurigaussian random fields,[33] are developed. These algorithms have potential to do reconstructions in a short duration and claimed to be applicable to (an)isotropic[31,32] or grading microstructures.[33] At present, the DCFs cannot be converged well to the true values, raising concerns in the accuracy in capturing multi-scale features in microstructure. More effort is needed in regard to pursuing an efficient reconstruction while preserving high accuracy.

In this work, the conventional two-point exchanging algorithm is improved to a highly practical level, capable of overcoming the above-mentioned limitations. We develop a multi-stage reconstruction process (Fig. 1) that first reconstructs the three-dimensional volume with a coarse resolution, then increases the resolution to finer levels stage-by-stage by breaking each voxel into multiple voxels of the same phase, followed by conducting

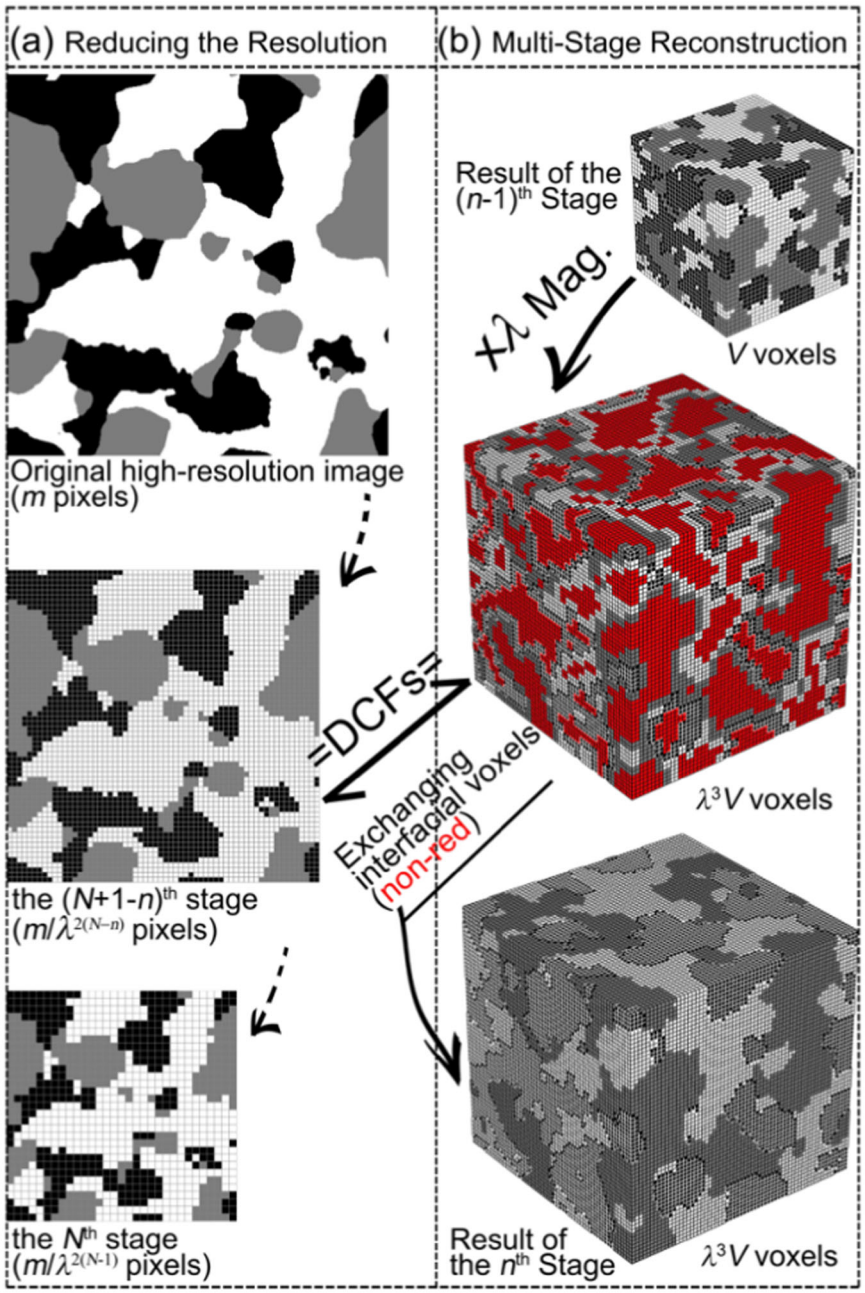

Fig. 1 Schematic of the distance correlation function (DCF) method. **a** *N*-stage deduction in resolution of the original high-resolution two-dimensional (2D) image of the microstructure. **b** the *N*-stage reconstruction of the 3D microstructure

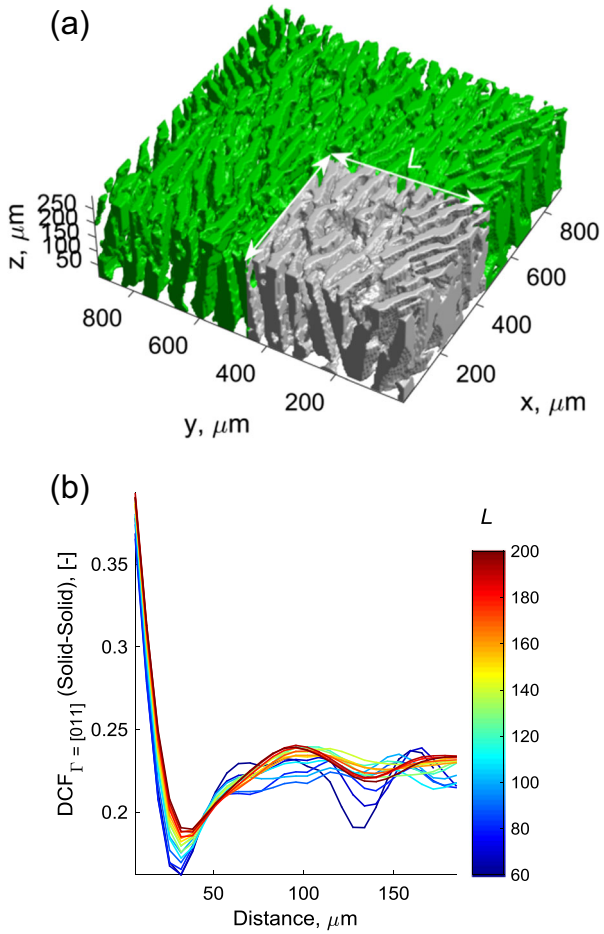

Fig. 2 Check of the representativeness of the three-dimensional (3D) X-ray micro-tomography (XMT) dataset consisting of 200-by-200-by-64 voxels for the porous Ni-YSZ electrode (green—solid, transparent—pores, voxel size = 4.5 μm) for determination of distance correlation functions (DCFs). **a** A cubic sub-domain with a side length of L is illustrated to study the effects of L on the DCFs. **b** The DCFs for solid–solid in the next-nearest neighbor (NNN) [011] direction calculated at different sizes (L) of the sub-domain, showing that the DCF is not changed obviously when $l > 160$ voxels

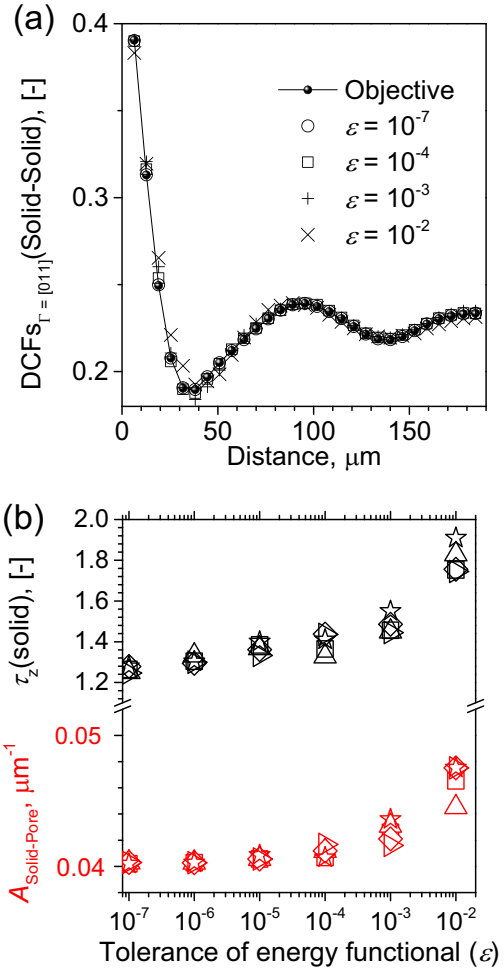

Fig. 3 Sweep of the energy tolerance to determine a rational value of the tolerance in this study. **a** The distance correlation functions (DCFs) of solid–solid in next-nearest neighbor (NNN) [011] direction determined from different energy tolerances and the true values of DCFs of the anisotropic porous anode from the X-ray micro-tomography (XMT) dataset. **b** The calculated tortuosity factor of the solid network along z-axis and solid–pore interface area as a function of the tolerance of energy functional. Five times 3D reconstructions are performed at each tolerance of relative error

two-point exchanging among only the interfacial voxels. Calculation of DCFs is fully optimized using a new mathematical model.

RESULTS

Mathematical methodology

A 2D micrograph can be represented by a $m_1 \times m_2$ matrix $\mathbf{M}^1_{2D}$, where the superscript "1" denotes the 1st/original image with a pixel size of δ. The various phases are distinguished by different integers in the matrix. The objective is to reconstruct a 3D image with a representative volume, say $m_1 \times m_2 \times m_3 \times \delta^3$, at the original resolution δ, while possessing nearly identical DCFs with $\mathbf{M}^1_{2D}$. To this end, a multi-stage downscaling of the 2D image followed by a multi-stage upscaling 3D reconstruction process is proposed. As illustrated in Fig. 1a, the 2D image is downscaled stage-by-stage by a factor of λ (typical 2) using nearest-neighbor (NN) interpolation. Thus, the resolution of the Nth stage coarsened 2D image $\mathbf{M}^N_{2D}$ is $\lambda^{N-1}\delta$, and the number of pixels is decreased to $m_1 \times m_2/\lambda^{2(N-1)}$, while the spatial area of image $m_1 \times m_2 \times \delta^2$ maintains unchanged. As illustrated in Fig. 1b, the final 3D image, $\mathbf{M}^N_{3D}$ can be reconstructed using an N-stage upscaling process that uses the DCFs of the $\mathbf{M}^N_{2D}, \ldots, \mathbf{M}^1_{2D}$ as the objective DCFs of the 1st, 2nd,…, Nth stage of the 3D reconstruction, successively. The 1st stage 3D image $\mathbf{M}^1_{3D}$ is obtained by exchanging voxels of a randomly generated 3D matrix with the same fractions of phases as in $\mathbf{M}^1_{2D}$ until its DCFs converge to that of $\mathbf{M}^N_{2D}$. To accelerate convergence, the two-point swaps are first performed among all the voxels (until a number of continuous failures) and then among the interfacial voxels that share edges/facets with different phase voxels. For the nth ($n > 1$) stage reconstruction, the $(n-1)$th stage $\mathbf{M}^{n-1}_{3D}$ is first upscaled by a factor of λ using NN interpolation, which is replacing each voxel with a $\lambda \times \lambda \times \lambda$ matrix of the same phase, as illustrated in Fig. 1b. Then, the DCFs of the upscaled $\mathbf{M}^{n-1}_{3D}$ are recalculated, and updated after each successful two-point exchanging, so that the DCFs converge to that of $\mathbf{M}^{N+1-n}_{2D}$. The voxels to be exchanged are selected only among the interfacial voxels, as shown in Fig. 1b. This will dramatically promote the computational efficiency because the interfacial voxels are only a small part of the whole, and the energy

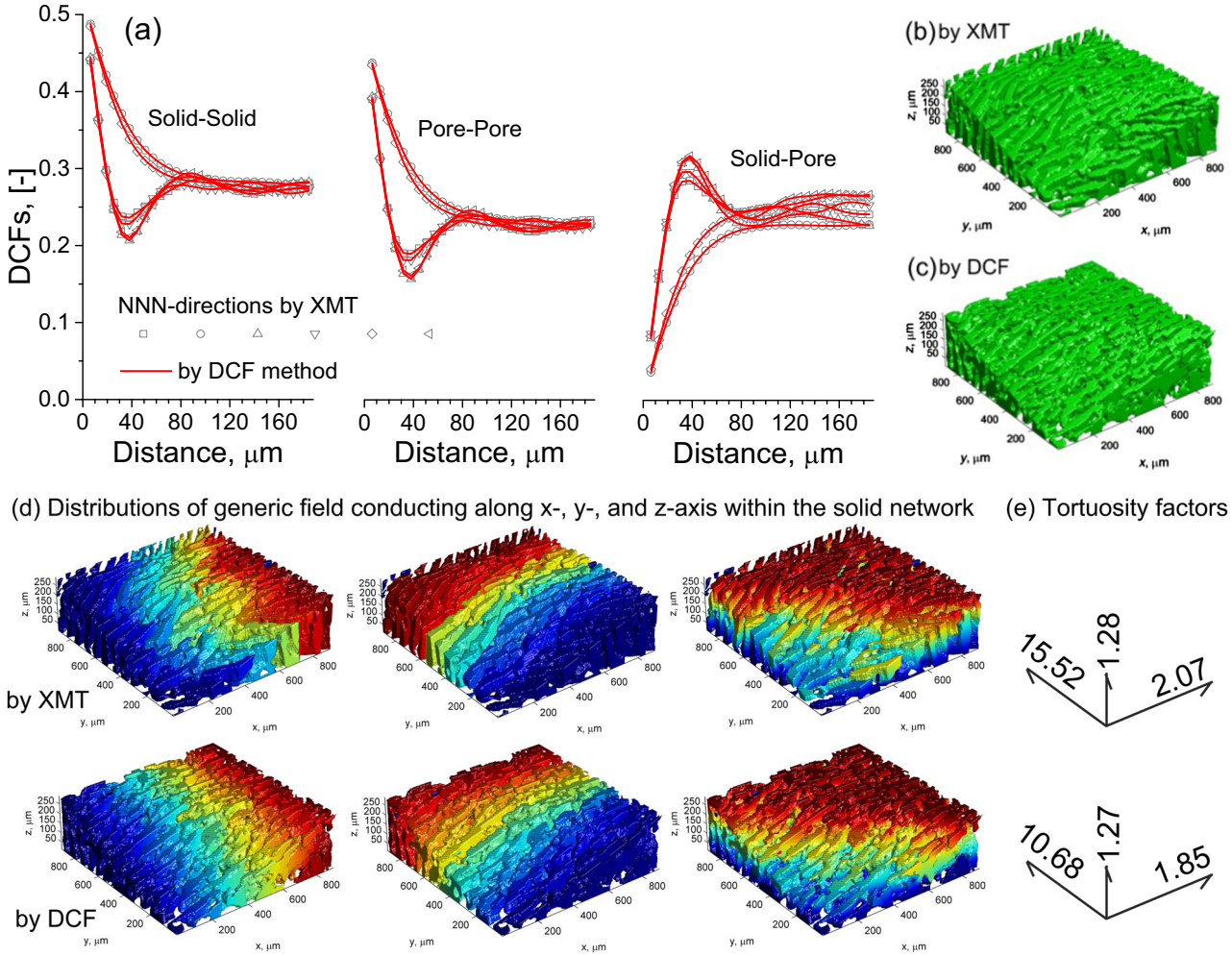

Fig. 4 Three-dimensional (3D) reconstruction of a porous anisotropic solid oxide fuel cell (SOFC) anode. **a** Comparison of distance correlation functions (DCFs) of solid–solid, pore–pore, solid–pore along the next-nearest neighbor (NNN) directions between the X-ray micro-tomography (XMT) **b** and the DCF **c** reconstructed microstructures. **d** Comparison between the generic field distributions conducting macroscopically along *x*-, *y*-, and *z*-axis directions within the XMT and DCF reconstructed microstructures by solving Laplace's equation of the generic field within the solid network with Dirichlet boundary conditions. **e** The tortuosity factors of the solid network along *x*-, *y*-, and *z*-axis of the XMT and DCF reconstructed microstructures. The voxel size is 4.5 μm. A corner is cropped off for showing the internal microstructure and the generic field

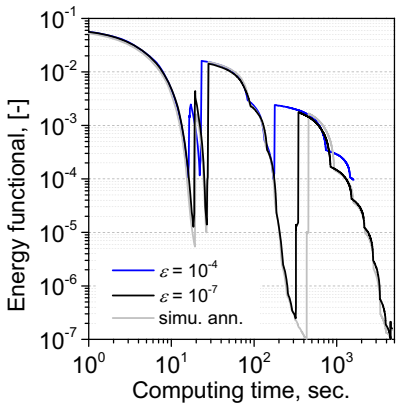

Fig. 5 Comparison on computing time. The energy functional of distance correlation functions (DCFs) as a function of computing time for the three-stage reconstructions with energy tolerances of 10^{-4} (blue) and 10^{-7} (black) and the three-stage reconstruction using a simulated annealing algorithm with a temperature of 10^{-8}/16 stage (gray) of the isotropic porous Ni-YSZ anode with a final dimension of 200-by-200-by-64 voxels

functional of DCFs is mainly derived from the interfacial regions. The isolated voxels are removed by random two-point swaps at the end of each stage. Once the DCFs are well converged, the 3D image is returned as the *n*th stage $\mathbf{M}^n_{3D}$.

For easy and efficient calculation, the DCFs can be defined in a vectorized fashion. In general, the DCF between phases *i* and *j* depends on directions if the microstructure is anisotropic. In analogy with the crystallographic directions of a cubic lattice, we consider the effects of the NN directions denoted by [100], [010], and [001], and the next-NN (NNN) directions denoted by [110], [1$\bar{1}$0], [101], [10$\bar{1}$], [011], and [01$\bar{1}$]. For the *n*th stage 3D image, represented by a $m_1/\lambda^{(N-n)} \times m_2/\lambda^{(N-n)} \times m_3/\lambda^{(N-n)}$ matrix $\mathbf{M}^n_{3D}$, the DCF between phases *i* and *j* along direction $\mathbf{\Gamma} = [\Gamma_1\Gamma_2\Gamma_3]$ can be defined by,

$$\mathrm{DCF}^n_{3D;i,j;\mathbf{\Gamma}}(m) = \left\langle \mathbf{M}^n_{3D;i;m\mathbf{\Gamma}} * \mathbf{M}^n_{3D;j;-m\mathbf{\Gamma}} \right\rangle, \quad (1)$$

The physical meaning of Eq. (1) is the probability of finding a vector $m\mathbf{\Gamma}$ within $\mathbf{M}^n_{3D}$ with the beginning and end voxels being, respectively, *i* and *j* phases. Herein, *m* denotes the distance in unit of voxel. The syntax "*" denotes element-by-element product of the two matrixes. The syntax "< >" denotes average value of elements. $\mathbf{M}^n_{3D;i;m\mathbf{\Gamma}}$ and $\mathbf{M}^n_{3D;j;-m\mathbf{\Gamma}}$ are direction dependent

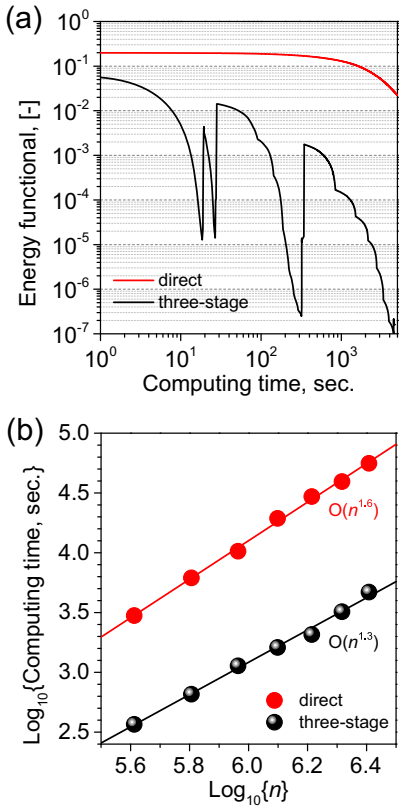

Fig. 6 Comparison on the computing efficiency and algorithm complexity for the direct one-stage and three-stage reconstructions of the anisotropic anode. **a** The energy functional of distance correlation functions (DCFs) as a function of computing time with an energy tolerances of 10^{-7}. **b** The computing time as a function of the total number of voxles (n) for the one-stage and the three-stage reconstructions, showing the computing complexities (Big O notation). Different numbers of voxels of the objective volumes are randomly selected sub-domains from the original X-ray micro-tomography (XMT) dataset

sub-matrixes of phases i and j, given by,

$$\mathbf{M}^n_{3D;i;\pm m\boldsymbol{\Gamma}} = \mathbf{M}^n_{3D;i}\left(\zeta^0_{\pm,1} : \zeta^1_{\pm,1}, \zeta^0_{\pm,2} : \zeta^1_{\pm,2}, \zeta^0_{\pm,3} : \zeta^1_{\pm,3}\right). \tag{2}$$

Herein, $\mathbf{M}^n_{3D;i}$ designates the matrix of phase i $\left(\mathbf{M}^n_{3D} = i\right)$, with the voxel value of 1 for phase i and 0 for the other phases. The indexes are given by,

$$\zeta^{\ell}_{\pm,k} = 1 - \ell + \ell m_k/\lambda^{N-n} \mp [\Gamma_k m \pm (2\ell - 1)\Gamma^2_k m]/2. \tag{3}$$

Equations (1)–(3) utilize all the voxels of $\mathbf{M}^n_{3D}$; therefore, giving a precious definition of DCFs. Exchanging two randomly selected voxels $\mathbf{v}_1$ and $\mathbf{v}_2$ of $\mathbf{M}^n_{3D}$ renews the DCFs by a increment of,

$$\Lambda^n_{3D;i,j;\boldsymbol{\Gamma}}(m) = \frac{\Delta^n_{i,j;\boldsymbol{\Gamma}}(\mathrm{v}_1, \mathrm{v}_2; m)}{\prod_k (m_k/\lambda^{N-n} - \Gamma^2_k m)}, \tag{4}$$

where

$$\Delta^n_{i,j;\boldsymbol{\Gamma}}(\mathrm{v}_1, \mathrm{v}_2; m) = \sum_{\substack{a,\,b\,=\,1,2;\,a\neq b \\ a,\,\beta\,=\,i,j;\,a\neq\beta}} \left[(\mathrm{v}_a) - (\mathrm{v}_b)_a\right](\mathrm{v}_b + (-1)^{\delta_{\beta i}} m\boldsymbol{\Gamma})_\beta. \tag{5}$$

Herein, $(\mathrm{v}_b + (-1)^{\delta_{\beta i}} m\boldsymbol{\Gamma})_\beta$ is 1 if the voxel $\mathrm{v}_b + (-1)^{\delta_{\beta i}} m\boldsymbol{\Gamma}$ belongs to phase β, and inside $\mathbf{M}^n_{3D}$, otherwise 0. $\delta_{\beta i}$ denotes the Kronecker function. Note that the vector $\mathbf{v}_1 - \mathbf{v}_2$ should not be in parallel with any of $\boldsymbol{\Gamma}$. Equation (5) is efficient for updating DCFs, because only the voxels $\boldsymbol{v}_{1,2} \pm m\boldsymbol{\Gamma}$ are involved in the calculation.

For isotropic microstructures, the DCFs are independent of directions, and thus can be given by the NN- or NNN-directional average,

$$\mathrm{DCF}^n_{3D;i,j;\Omega}(m) = \left\langle \mathbf{M}^n_{3D;i;m\boldsymbol{\Gamma}} * \mathbf{M}^n_{3D;j;-m\boldsymbol{\Gamma}} : \boldsymbol{\Gamma} \in \Omega \right\rangle. \tag{6}$$

where Ω denotes "NN" or "NNN". Statistically, we have $\mathrm{DCF}^n_{3D;i,j;\mathrm{NN}}(\sqrt{2}m) = \mathrm{DCF}^n_{3D;i,j;\mathrm{NNN}}(m)$. However, in order to avoid cuboid-shaped patterns in the reconstruction, both the NN- and NNN-directional DCFs are considered here. Exchanging voxels $\mathbf{v}_1$ and $\mathbf{v}_2$ renews the DCFs by a increment of,

$$\Lambda^n_{3D;i,j;\Omega}(m) = \frac{\sum_{\boldsymbol{\Gamma}\in\Omega} \Delta^n_{i,j;\boldsymbol{\Gamma}}(\mathrm{v}_1, \mathrm{v}_2; m)}{\sum_{\boldsymbol{\Gamma}\in\Omega} \prod_k (m_k/\lambda^{N-n} - \Gamma^2_k m)}. \tag{7}$$

Above equations are applicable to 2D images ($m_3 = 1$). Therefore, the target $\mathrm{DCF}^{N+1-n}_{2D;i,j;\boldsymbol{\Gamma}}(m)$ of the nth stage reconstruction can be calculated using Eqs. (1) or (6). The global objective is to minimize the energy functional, defined by,

$$\varepsilon = \frac{1}{\max(m)} \sum_{i,j,\boldsymbol{\Gamma},m} \left(\log_{10}\mathrm{DCF}^n_{3D;i,j;\boldsymbol{\Gamma}}(m) - \log_{10}\mathrm{DCF}^{N+1-n}_{2D;i,j;\boldsymbol{\Gamma}}(m)\right)^2. \tag{8}$$

Herein, the Monte-Carlo Metropolis rule (e.g., simulated annealing temperature) is not used. That is, the two-point exchange is accepted only if the energy functional is decreased. This strategy avoids calibration of the simulated annealing temperature. The risk of getting trapped in a local minimum of the energy functional probably induced by this strategy can be suppressed effectively by the multi-stage method. In addition, the convergence seems not be accelerated obviously by a simulated annealing strategy, as will be demonstrated later. However, one can easily introduce a Monte-Carlo Metropolis rule if necessary. Note that logarithmic DCFs are used in the energy functional since they are sensitive to the tiny variations in the DCFs, especially with small values, and therefore effective to capture the fine features of interfaces and the phase distributions with small volume fractions. The two-point exchanging for each stage is continued until the energy functional is decreased to a sufficiently small tolerance, or the energy functional is not decreased after a number of continuous attempts of two-point exchanging. The algorithm is realized using MATLAB.

Validation by a X-ray micro-tomography dataset

The DCF method is first verified using the X-ray micro-tomography (XMT) dataset of an anisotropic porous anode support with a dimension of $200 \times 200 \times 64$ voxels and a voxel size of 4.5 μm, published in our prior study.[34] This dimension is shown to be representatively large for determination of the DCFs (Fig. 2). A three-stage downscaling of the dataset is performed so that the XMT dataset is finally downscaled to $50 \times 50 \times 16$ voxels. For each stage of downscaling, the objective NN- and NNN-directional DCFs for the binary pairs of solid-solid, pore-pore, and solid-pore are calculated using Eq. (1). Then, the 3D microstructure of the anode with a final dimension of $200 \times 200 \times 64$ voxels is reconstructed using a three-stage reconstruction, implemented in a 2.8 GHz, 16GB RAM computer. Geometric properties of the 3D volumes are calculated using the algorithms we reported in refs [35,36]. First of all, the tolerance of energy functional should be determined. It is shown in Fig. 3a that the fitting goodness of the reconstructed DCFs under an energy tolerance of 10^{-4} seems higher than the results in refs [31–33], where macroscopic departures from the true values are presented. However, under this tolerance, the

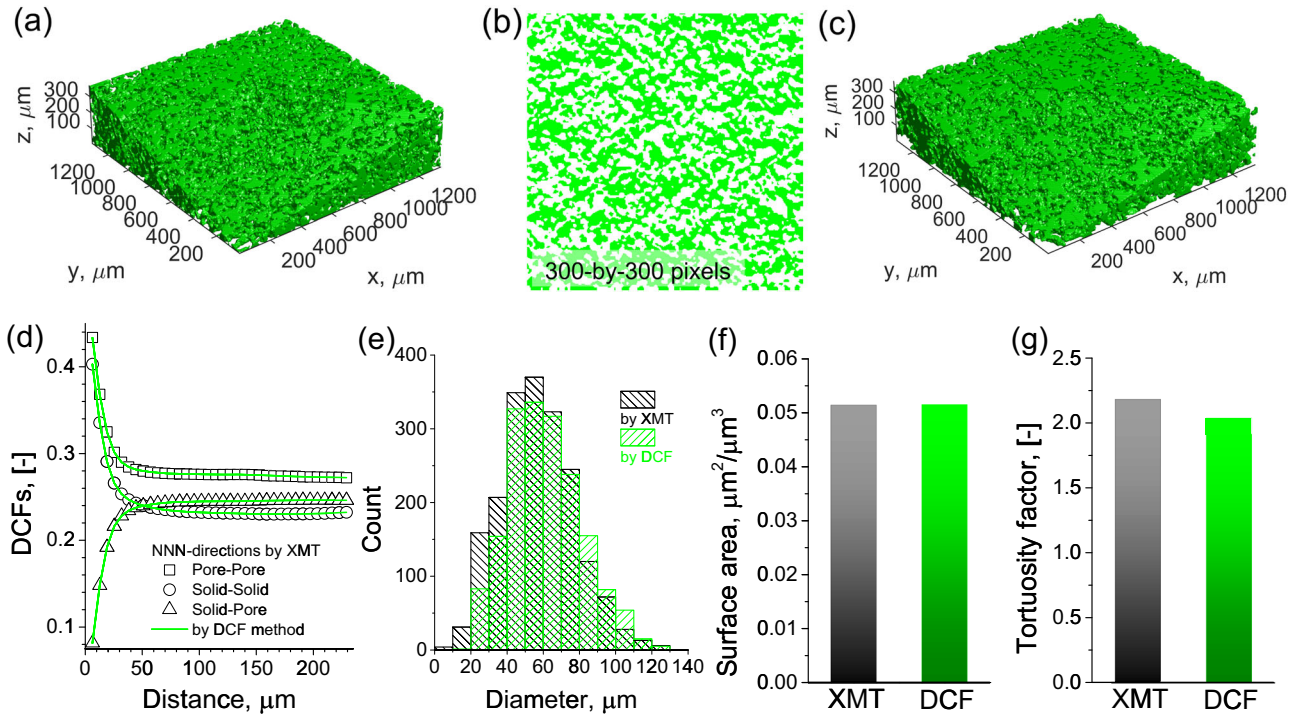

Fig. 7 Three-dimensional (3D) reconstruction of a porous isotropic solid oxide fuel cell (SOFC) anode. **a** The X-ray micro-tomography (XMT) dataset for the anode with a spatial resolution of 4.5 μm. **b** A representative 2D slice from the XMT dataset as the input micrograph of the multi-stage reconstruction. **c** The reconstructed microstructure by a three-stage reconstruction. The solid phase and pores are represented by green and transparent networks respectively in **a**–**c**. A corner is cropped off for showing the internal microstructure in **a** and **c**. **d** Comparison of distance correlation functions (DCFs) of solid–solid, pore–pore, solid–pore along the NNN directions between the XMT and the DCF method. **e**–**g** Comparison of key geometric characteristics including distribution of particle diameters **e**, internal surface area **f**, and tortuosity factor **g** of the solid phase between the XMT and the DCF method

solid-pore interfacial area and the tortuosity factor of the solid network are systematically overestimated and scatter significantly (Fig. 3b). Thus, a lower tolerance of 10^{-7} is used to guarantee a high accuracy of evaluation of geometric properties. Under this tolerance, the small dispersion of geometric properties indicates a good robustness of the algorithm. Figure 4 shows the typical reconstruction results, showing that the DCFs along the six NNN directions of the reconstructed microstructure are converged well to those of the XMT dataset (Fig. 4a). The 3D microstructures by the XMT (Fig. 4b) and the DCF method (Fig. 4c) show that the reconstructed microstructure is not exactly a duplicate of the real microstructure. The DCFs are in nature reduce-dimension descriptors of microstructures, and thus cannot reproduce the real microstructure, but generate a microstructure that has the same statistical significance of geometric properties with the real microstructure. The solid-pore interfacial areas by the XMT and the DCF method are very close, being 0.040 and 0.042 $\mu m^2/\mu m^3$, respectively. The anisotropy of the anode support is evaluated using tortuosity factors along *x*-, *y*-, and *z*-axis, showing that the distributions of the generic field conducting along *x*-, *y*-, and *z*-axis by the DCF method are similar with that by the XMT (Fig. 4d). The tortuosity factors along *x*-, *y*- and *z*-axis by the DCF method are in good agreement with those by the XMT (Fig. 4e). The computing duration under the energy tolerance of 10^{-7} is about 1.3 h, which is not further accelerated by a simulated annealing strategy (Fig. 5). Note that the duration under the energy tolerance of 10^{-4} is quite short, only about 0.4 h (Fig. 5), which is, however, inadvisable due to the low accuracy (Fig. 3). In addition, we attempt to directly reconstruct the $200 \times 200 \times 64$ volume by a one-stage reconstruction (as defined in the section of Mathematical methodology) where two-point swaps are randomly selected among all the voxels. However, the energy functional is not decreased obviously after 1.3 h running (Fig. 6a). The accelerated convergence using the multi-stage protocol is attributed to the following three contributions: (1) the two-point exchange is performed among only the interfacial voxels, only a small portion of the bulk; (2) the exchange is highly likely accepted since the downscaling usually degrades the quality interfaces and the energy functional derives mainly from the interfacial regions; (3) the calculation (Eq. 1) and the update (Eq. 4) of DCFs are vectorized, so that the computational efficiency is promoted. Technically, the efficiency could be further increased by employing a compiled language, such as C++ or Fortran. We further compare the computational complexities of the three-stage and the one-stage protocols by plotting the computing time as a function of the total number of voxels (n). As shown in Fig. 6b, the complexity of the one-stage protocol is about $O(n^{1.6})$. However, the multi-stage protocol has a lower complexity of $O(n^{1.3})$. Thus, the multi-stage protocol permits a high-throughput reconstruction, showing the feasibility of reconstructing bigger volumes. The algorithm can tackle substantial material phases, although the presented case is a two-phase microstructure.

DISCUSSION

The applicability and the high-throughput merit of the multi-stage reconstruction method is further verified by the XMT dataset of an isotropic porous SOFC anode. The dataset has a dimension of

$300 \times 300 \times 80$ voxels with a voxel size of 4.5 μm (see the Methods for 3D imaging). The 3D microstructure is shown in Fig. 7a, where the solid phase (green) and pores (transparent) are segmented. A representative 2D slice with a dimension of 300×300 pixels (Fig. 7b) is selected from the dataset for use of the input 2D micrograph of the multi-stage 3D reconstruction. A three-stage reconstruction is performed with a target dimension of $300 \times 300 \times 80$ voxels, and is accomplished within 10.3 h. The reconstructed microstructure (Fig. 7c) is very similar to the XMT measurements (Fig. 7a). The DCFs are converged nicely to the objective values, without detectable fitting errors (Fig. 7d). In addition, the key geometric characteristics are well recovered by the multi-stage reconstruction. As shown in Fig. 7e–g, the reconstructed distribution of particle diameters (Fig. 7e), internal surface area (Fig. 7f) and tortuosity factor (Fig. 7g) of the solid phase agree quantitatively with those of the XMT dataset.

The above discussion provides a demonstration of reconstructing representatively large-sized 3D microstructures from 2D micrograph alone. The multi-stage 3D reconstruction based on DCFs opens an economic, easy-to-use, and high-throughput path for quantifying the stochastic heterogeneous microstructures. Although the present results are focused on SOFC electrodes, this approach is generally applicable to a wide range of isotropic and anisotropic microstructures, and can also be extended to understand the correlations between processing, microstructure, and performance.

METHODS

Reconstruction of the isotropic SOFC anode by XMT

The isotropic SOFC anode substrate was first fabricated by mixing of powders (NiO, Ga-doped ceria, graphite) followed by dry-pressuring and sintering process.[2] Xradia X-ray tomographic microscope (Xradia Inc., Micro-XCT400) was then used to image the 3D microstructure of the anode substrate, under a source setting of 140 kV and 70 mA with an exposure time of 1.5 s per radiograph. The source-rotation axis (RA) distance was 40 mm, and the detector-RA distance was 20 mm. The pixel size was 4.5 μm. The optical magnification was ×4. Then, anisotropic diffusion smoothing was applied on the raw XMT micrographs to eliminate noise. The solid phase and pores were segmented using a watershed algorithm.

Code availability

A version of software written with MATLAB for the multi-stage reconstruction method is available from the authors upon reasonable request.

DATA AVAILABILITY

The data supporting the results are available from the authors upon reasonable request.

ACKNOWLEDGEMENTS

We gratefully acknowledge the financial support from Natural Science Foundation of China (21673062, 51402066, and 51371070), China Postdoctoral Science Foundation funded project (2015M571411, 2016T90282, LBH-Z15061, and LBH-TZ1607), and the US Department of Energy SECA Core Technology Program (DE-FE0031670).

AUTHOR CONTRIBUTIONS

Y.Z. and M.Y conceived the project. Y.Z. developed the method and wrote the draft. Y.W., Z.J., Y.C., F.C., C.X., and M.N. revised the draft. Y.Z. and Y.C. prepared the isotropic anode and performed the 3D imaging by XMT.

ADDITIONAL INFORMATION

Competing interests: The authors declare no competing interests.

Publisher's note: Springer Nature remains neutral with regard to jurisdictional claims in published maps and institutional affiliations.

REFERENCES

1. Minh, N. Q. Ceramic fuel cells. *J. Am. Ceram. Soc.* **76**, 563–588 (1993).
2. Shao, Z., Zhou, W. & Zhu, Z. Advanced synthesis of materials for intermediate-temperature solid oxide fuel cells. *Prog. Mater. Sci.* **57**, 804–874 (2012).
3. Jiang, S. P. Nanoscale and nano-structured electrodes of solid oxide fuel cells by infiltration: advances and challenges. *Int. J. Hydrog. Energy* **37**, 449–470 (2012).
4. Vohs, J. M. & Gorte, R. J. High-performance SOFC cathodes prepared by infiltration. *Adv. Mater.* **21**, 943–956 (2009).
5. Ding, D., Li, X., Lai, S. Y., Gerdes, K. & Liu, M. Enhancing SOFC cathode performance by surface modification through infiltration. *Energ. Environ. Sci.* **7**, 552–575 (2009).
6. Mahato, N., Banerjee, A., Gupta, A., Omar, S. & Balani, K. Progress in material selection for solid oxide fuel cell technology: a review. *Prog. Mater. Sci.* **72**, 141–337 (2015).
7. Mogensen, M., Høgh, J., Hansena, K. V. & Jacobsen, T. A critical review of models of the H_2/H_2O/Ni/SZ electrode kinetics. *ECS Trans.* **7**, 1329–1338 (2007).
8. Zhang, Y., Ni, M., Xia, C. & Chen, F. A sintering kinetics model for ceramic dual-phase composite. *J. Am. Ceram. Soc.* **97**, 2580–2589 (2014).
9. Zhang, Y., Ni, M. & Xia, C. Microstructural insights into dual-phase infiltrated solid oxide fuel cell electrodes. *J. Electrochem. Soc.* **160**, F834–F839 (2013).
10. Jiang, S. et al. The electrochemical performance of LSM/zirconia–yttria interface as a function of a-site non-stoichiometry and cathodic current treatment. *Solid State Ion* **121**, 1–10 (1999).
11. Jiang, S. P. & Love, J. G. Origin of the initial polarization behavior of Sr-doped $LaMnO_3$ for O_2 reduction in solid oxide fuel cells. *Solid State Ion* **138**, 183–190 (2001).
12. Zhang, Y., Chen, K., Xia, C., Jiang, S. P. & Ni, M. A model for the delamination kinetics of $La_{0.8}Sr_{0.2}MnO_3$ oxygen electrodes of solid oxide electrolysis cells. *Int. J. Hydrogen Energy* **37**, 13914–13920 (2012).
13. Zhang, Y. & Xia, C. A particle-layer model for solid-oxide-full-cell cathodes with different structures. *J. Power Sources* **195**, 4206–4212 (2010).
14. Irvine, J. T. S. et al. Evolution of the electrochemical interface in high-temperature fuel cells and electrolysers. *Nat. Energy* **1**, 15014 (2016).
15. Cocco, A. P. et al. Three-dimensional microstructural imaging methods for energy materials. *Phys. Chem. Chem. Phys.* **15**, 16377–16407 (2013).
16. Zhang, Y., Ma, J. & Yan, M. Is 2D stereological method good enough for quantification of solid oxide fuel cell electrode microstructure? *Sci. Bull.* **61**, 1313–1316 (2016).
17. Wilson, J. R. et al. Three-dimensional reconstruction of a solid-oxide fuel-cell anode. *Nat. Mater.* **5**, 541 (2006).
18. Grew, K. N. et al. Nondestructive nanoscale 3D elemental mapping and analysis of a solid oxide fuel cell anode. *J. Electrochem. Soc.* **157**, B783–B792 (2010).
19. Lin, Y., Fang, S., Su, D., Brinkman, K. S. & Chen, F. Enhancing grain boundary ionic conductivity in mixed ionic-electronic conductors. *Nat. Commun.* **6**, 6824 (2014).
20. Brunello, G. et al. Quantitative interpretation of impedance spectroscopy data on porous LSM electrodes using X-ray computed tomography and Bayesian model-based analysis. *Phys. Chem. Chem. Phys.* **19**, 25334–25345 (2017).
21. Epting, W. et al. Quantifying intermediate frequency heterogeneities of SOFC electrodes using X-ray computed tomography. *J. Am. Ceram. Soc.* **100**, 2232–2242 (2017).
22. Jiao, Z. & Shikazono, N. 3D reconstruction size effect on the quantification of solid oxide fuel cell nickel–yttria-stabilized-zirconia anode microstructural information using scanning electron microscopy-focused ion beam technique. *Sci. Bull.* **61**, 1317–1323 (2016).
23. Quiblier, J. A. A new three-dimensional modeling technique for studying porous media. *J. Colloid Interface Sci.* **98**, 84–102 (1984).
24. Lu, B. & Torquato, S. *n*-point probability functions for a lattice model of heterogeneous media. *Phys. Rev. B* **42**, 4453–4459 (1990).
25. Yeong, C. L. Y. & Torquato, S. Reconstructing random media. *Phys. Rev. E* **57**, 495–506 (1998).
26. Yeong, C. L. Y. & Torquato, S. Reconstructing random media. II. Three-dimensional media from two-dimensional cuts. *Phys. Rev. E* **58**, 224–233 (1998).
27. Manwart, C., Torquato, S. & Hilfer, R. Stochastic reconstruction of sandstones. *Phys. Rev. E* **62**, 893–899 (2000).
28. Jiao, Y., Stillinger, F. H. & Torquato, S. Modeling heterogeneous materials via two-point correlation functions: basic principles. *Phys. Rev. E* **76**, 031110 (2007).
29. Jiao, Y., Stillinger, F. H. & Torquato, S. Modeling heterogeneous materials via two-point correlation functions. II. Algorithmic details and applications. *Appl. Phys. Rev. E* **77**, 031135 (2008).
30. Suzue, Y., Shikazono, N. & Kasagi, N. Micro modeling of solid oxide fuel cell anode based on stochastic reconstruction. *J. Power Sources* **184**, 52–59 (2008).

31. Baniassadi, M. et al. Three-phase solid oxide fuel cell anode microstructure realization using two-point correlation functions. *Acta Mater.* **59**, 30–43 (2011).
32. Sundararaghavan, V. Reconstruction of three-dimensional anisotropic microstructures from two-dimensional micrographs imaged on orthogonal planes. *Integr. Mater. Manuf. Innov.* **3**, 19–29 (2014).
33. Moussaoui, H. et al. Stochastic geometrical modeling of solid oxide cells electrodes validated on 3D reconstructions. *Comput. Mater. Sci.* **143**, 262–276 (2018).
34. Chen, Y. et al. Direct-methane solid oxide fuel cells with hierarchically porous Ni-based anode deposited with nanocatalyst layer. *Nano Energy* **10**, 1–9 (2014).
35. Zhang, Y., Xia, C. & Ni, M. Simulation of sintering kinetics and microstructure evolution of composite solid oxide fuel cells electrodes. *Int. J. Hydrogen Energy* **37**, 3392–3402 (2012).
36. Zhang, Y., Sun, Q., Xia, C. & Ni, M. Geometric properties of nanostructured solid oxide fuel cell electrodes. *J. Electrochem. Soc.* **160**, F278–F289 (2013).

Open Access This article is licensed under a Creative Commons Attribution 4.0 International License, which permits use, sharing, adaptation, distribution and reproduction in any medium or format, as long as you give appropriate credit to the original author(s) and the source, provide a link to the Creative Commons license, and indicate if changes were made. The images or other third party material in this article are included in the article's Creative Commons license, unless indicated otherwise in a credit line to the material. If material is not included in the article's Creative Commons license and your intended use is not permitted by statutory regulation or exceeds the permitted use, you will need to obtain permission directly from the copyright holder. To view a copy of this license, visit http://creativecommons.org/licenses/by/4.0/.

© The Author(s) 2019